Corrected mean-field models for spatially dependent advection-diffusion-reaction phenomena

Matthew J. Simpson[1,2] and Ruth E. Baker[3]

[1]*Mathematical Sciences, Queensland University of Technology, Brisbane, Australia*

[2]*Tissue Repair and Regeneration Program, Institute of Health and Biomedical Innovation (IHBI), Queensland University of Technology, Brisbane, Australia*

[3]*Centre for Mathematical Biology, Mathematical Institute, University of Oxford, 24-29 St Giles', Oxford, OX1 3LB, United Kingdom*

(Received 20 January 2011; revised manuscript received 27 February 2011; published 26 May 2011)

In the exclusion-process literature, mean-field models are often derived by assuming that the occupancy status of lattice sites is independent. Although this assumption is questionable, it is the foundation of many mean-field models. In this work we develop methods to relax the independence assumption for a range of discrete exclusion-process-based mechanisms motivated by applications from cell biology. Previous investigations that focused on relaxing the independence assumption have been limited to studying initially uniform populations and ignored any spatial variations. By ignoring spatial variations these previous studies were greatly simplified due to translational invariance of the lattice. These previous corrected mean-field models could not be applied to many important problems in cell biology such as invasion waves of cells that are characterized by moving fronts. Here we propose generalized methods that relax the independence assumption for spatially inhomogeneous problems, leading to corrected mean-field descriptions of a range of exclusion-process-based models that incorporate (i) unbiased motility, (ii) biased motility, and (iii) unbiased motility with agent birth and death processes. The corrected mean-field models derived here are applicable to spatially variable processes including invasion wave-type problems. We show that there can be large deviations between simulation data and traditional mean-field models based on invoking the independence assumption. Furthermore, we show that the corrected mean-field models give an improved match to the simulation data in all cases considered.

DOI: 10.1103/PhysRevE.83.051922 PACS number(s): 87.10.Rt, 87.17.Aa, 87.17.Jj

I. INTRODUCTION

Deriving accurate mean-field models corresponding to particular discrete reactive transport phenomena is important in many disciplines including fluid mechanics [1,2], ecology [3–5], and cell biology [6–14]. In particular, cell biology demands that mathematical models be formulated to describe the behavior of individual cells, including events such as motility, proliferation, and death. This is important because modern time-lapse data and other imaging techniques typically focus on describing and measuring stochastic, cell-level events and properties [11]. Understanding the relationship between particular discrete mechanisms and their associated mean-field descriptions is essential for our comprehension of how particular changes in cell-level properties manifest in population-level descriptions of the system.

To derive an appropriate mean-field description of a particular stochastic system, a number of simplifying assumptions are usually made. We will describe these simplifying assumptions with reference to Fig. 1. Suppose that the one-dimensional lattice in Fig. 1 represents a snapshot of an unbiased exclusion process. Each lattice site is indexed l, where $l \in \mathbb{Z}^+$, and the lattice spacing is Δ, so that each site has position $l\Delta$.

The dynamics of the system will evolve according to the following mechanism. Each agent will attempt to step to a nearest neighbor lattice site with the probability of movement per unit time P_m. The direction of movement will be unbiased so that a motile agent will attempt to move left and right with equal probability of $1/2$. Motility events will be successful if the target site is unoccupied. If the target site is occupied then that particular motility event will be aborted. For example, in Fig. 1 the agent at site $l+3$ is able to move to either of its neighboring sites, whereas the agent at site l is only able to move to the right since site $l-1$ is occupied. One way to simulate this procedure is to implement the algorithm with constant time steps of length τ so that each computational time step advances time from t to $t+\tau$ [8,9]. To obtain a mean-field description of this mechanism we introduce C_l^* to represent the occupancy of the lth lattice site. In any single realization of the stochastic model $C_l^* = 1$ when the lth lattice site is occupied, while $C_l^* = 0$ when the lth lattice site is vacant. By averaging the occupancy of each site over many identically prepared realizations we obtain $\langle C_l^* \rangle = C_l \in [0,1]$ which is the average occupancy of the lth lattice site. To develop a macroscopic description of the microscopic mechanism, we consider the continuous-time limit as $\tau \to 0$ and form a conservation statement describing the rate of change of C_l:

$$\frac{\mathrm{d}C_l}{\mathrm{d}t} = \frac{P_m}{2}[C_{l-1}(1-C_l) + C_{l+1}(1-C_l) - C_l(1-C_{l-1}) - C_l(1-C_{l+1})]. \quad (1)$$

Positive terms on the right of Eq. (1) represent motility events that increase the average occupancy of site l and negative terms represent events that decrease the average occupancy of site l. Each term on the right of Eq. (1) has three factors which have a straightforward physical interpretation. The factors in the first term on the right of Eq. (1) consist of: (i) $P_m/2$, the probability per unit time that an agent attempts to step from site $l-1$ to site l; (ii) C_{l-1}, the probability that site $l-1$ is occupied at time t; and (iii) $(1-C_l)$, the probability that site l is vacant at time t. We interpret the product $P_m C_{l-1}(1-C_l)/2$ as the net probability of a movement from site $l-1$ to site l per

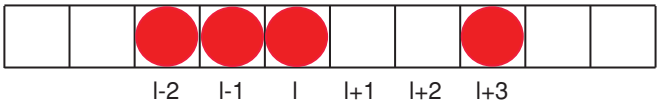

FIG. 1. (Color online) Exclusion process schematic. The exclusion process takes place on a one-dimensional lattice and each site can be occupied by, at most, one agent. At the particular instant shown, occupied sites are denoted with a dot while vacant sites are empty. Agents move with probability P_m per unit time. Attempted motility events that would place an agent on an already occupied site are aborted.

unit time. Given that we interpret the product of probabilities as a net transition probability implies that we are assuming that the occupancy status of site $l-1$ is independent of the occupancy status of site l. This assumption is also required to arrive at the remaining three terms on the right of Eq. (1). Although this assumption appears questionable [15], it is the foundation of many mean-field models in the exclusion process literature [6,8–11,13]. Proceeding with this assumption we see that Eq. (1) simplifies to

$$\frac{\mathrm{d}C_l}{\mathrm{d}t} = \frac{P_m}{2}[C_{l-1} - 2C_l + C_{l+1}], \tag{2}$$

which is a semidiscrete linear diffusion equation. This is a well-known result [8,9,15]. Previous computational studies have confirmed that simulation data from an unbiased exclusion process matches the solution of the linear diffusion equation extremely well for a wide range of initial conditions [8,9,11]. Although computational simulations appear to confirm the validity of Eq. (2), the arguments leading to Eq. (2) are approximate only and rely on invoking the independence assumption. Liggett emphasised the approximate nature of these arguments, referring to this level of analysis as heuristic [15], pp. 222–223.

As we have pointed out, many computational simulations support the validity of Eq. (2). However, several other studies have considered extensions to the unbiased motility mechanism, namely biased motility [6,11] and unbiased motility with proliferation [10,16], and have shown that traditional mean-field models based on similar independence assumptions do not always match the discrete data. At present we have no formal method of understanding why certain discrete models are insensitive to the independence assumption, whereas others appear to be affected in some way by the independence assumption.

The aim of this work is to develop computationally tractable methods that relax the independence assumptions underlying the mean-field descriptions of a range of discrete exclusion-process-based mechanisms. This work will provide a platform to test whether or not the independence assumption is valid. In situations where the independence assumption is invalid, our analysis allows us to determine the magnitude of various correlation functions, thereby giving a quantitative measure of how poor the independence assumption is for that particular situation. To achieve this we study the k-point distribution functions $\rho^{(k)}\,(k = 1,2,3,\ldots)$ [17,18] for various exclusion process models. This procedure leads to a system of coupled nonlinear equations describing the evolution of the k-point distribution functions for each site on the lattice and avoids the need for any independence assumptions. To solve this system of equations in general we must truncate the system using a moment closure approximation. For this study we use a standard moment closure approximation called the Kirkwood superposition approximation (KSA) [3–5,14,17–20].

Previous investigations using this approach have been limited to studying initially uniform populations [5,14,17,18]. By focusing only on initially uniform problems, these previous studies were greatly simplified due to translational invariance of the lattice. These previous uniform population studies focused on modeling the evolution of the total size of the population only, without any regard to the spatial distribution of the population, and could not be applied to many important problems in cell biology. For example, invasion wave phenomena involves a population of cells that are motile and proliferative. Invasion waves of cells are typically characterized by constant-speed fronts which move into uninvaded tissues [21,22]. The previous studies that focused on spatially uniform populations could not be applied to study invasion wave phenomena. Here we introduce generalized techniques that deal with spatially variable reactive transport processes including invasion wave-type problems. We show how to use k-point distribution functions and the KSA closure approximation to develop improved mean-field models of these processes.

In summary, we prove that the mean-field model for unbiased motility is governed exactly by Eq. (1) which means that the independence assumption leads to an exact result by coincidence. This explains why simulation data always matches up with a solution of the linear diffusion equation for simple unbiased motility. For biased motility we show that small deviations between the standard mean-field model and discrete data are corrected using an improved KSA-based model. These new results show that the independence assumption is inappropriate for biased motility. For unbiased motility with agent proliferation and death, we show that there can be very large deviations between the standard mean-field model and discrete data, indicating that the independence assumption is grossly inadequate for agent proliferation and death processes. In all cases the KSA-based mean-field result gives an improved match to the simulation data relative to the traditional mean-field result. All of these new results are relevant to situations where the agent density varies spatially across the lattice. This means that our new results are applicable to a much wider range of problems than previous studies which have ignored spatial effects [5,14,17,18].

II. ANALYSIS

To make progress we define the k-point distribution functions $\rho^{(k)}\,(k = 1,2,3,\ldots)$ for several different kinds of motility, birth and death events on a one-dimensional lattice in the context of an exclusion process. The k-point distribution functions are multivariate probability distribution functions describing the occupancy of k-tuplets of lattice sites. We will use l and m to refer to the lth and mth lattice sites and we define the lattice variable $\sigma_l \in \{0, A\}$ to represent the state of the lth lattice site, so that $\sigma_l = 0$ indicates that site l is vacant and $\sigma_l = A$ indicates that site l is occupied.

For $k = 1$ the distribution function is a univariate distribution describing the total density of agents on site l,

$$\rho^{(1)}(A_l) = C_l, \quad \rho^{(1)}(0_l) = 1 - C_l, \tag{3}$$

where C_l is the average occupancy of site l. This simply means that $\rho^{(1)}(A_l)$ is the probability of finding an agent at site l.

For $k = 2$ the distribution function is a bivariate distribution. To define this distribution we make use of correlation functions that can be written as

$$F_{\lambda,\mu}(l,m) = \frac{\rho^{(2)}(\sigma_l,\sigma_m)}{\rho^{(1)}(\sigma_l)\rho^{(1)}(\sigma_m)}, \tag{4}$$

for $l \neq m$, with λ and μ denoting the state of sites l and m, respectively [14,17,18]. These correlation functions provide the key ingredient allowing us to relax the independence assumptions that underpin the traditional mean-field approach demonstrated in Sec. I. By setting $F_{\lambda,\mu}(l,m) \equiv 1$ we are assuming the occupancy status of sites l and m to be independent which is consistent with the traditional mean-field approach. Instead, our approach allows us to formulate an improved mean-field model by allowing the correlation functions to evolve as part of the model solution. This approach inherently relaxes the independence assumption and gives us a quantitative measure of the importance of correlation effects in various exclusion process models.

We now define a relationship between different kinds of correlation functions, $F_{\lambda,\mu}(l,m)$, for different states λ and μ. By summing over the states of lattice sites we can write down relationships between $\rho^{(2)}$ and $\rho^{(1)}$, given by

$$\sum_{\sigma_m} \rho^{(2)}(\sigma_l,\sigma_m) = \rho^{(1)}(\sigma_l). \tag{5}$$

For example, we see that

$$\rho^{(2)}(A_l,A_m) + \rho^{(2)}(A_l,0_m) = \rho^{(1)}(A_l). \tag{6}$$

Combining Eqs. (4) and (6) we obtain a relationship between $F_{A,0}(l,m)$ and $F_{A,A}(l,m)$ given by

$$F_{A,0}(l,m) = \frac{1 - \rho^{(1)}(A_m)F_{A,A}(l,m)}{1 - \rho^{(1)}(A_m)}. \tag{7}$$

By following the same procedure and considering the sum $\rho^{(2)}(A_l,A_m) + \rho^{(2)}(0_l,A_m) = \rho^{(1)}(A_m)$, we obtain a relationship between $F_{0,A}(l,m)$ and $F_{A,A}(l,m)$ given by

$$F_{0,A}(l,m) = \frac{1 - \rho^{(1)}(A_l)F_{A,A}(l,m)}{1 - \rho^{(1)}(A_l)}. \tag{8}$$

With these definitions we can construct the systems of master equations for particular motility, proliferation, and death mechanisms. We will now consider several different cases separately to understand how the correlation analysis extends and informs the previous heuristic analysis obtained by invoking the independence assumptions.

III. RESULTS

A. Unbiased motility

We first consider the most straightforward case where an isolated agent at site l attempts to step to sites $l \pm 1$ with equal probability of $1/2$. The probability per unit time of a motility event is P_m, and attempted motility events that would place an agent on an occupied site are aborted. Incorporating this mechanism we can write down the evolution equation for $\rho^{(1)}(A_l)$ as follows:

$$\begin{aligned}\frac{\mathrm{d}\rho^{(1)}(A_l)}{\mathrm{d}t} &= \frac{P_m}{2}[\rho^{(2)}(A_{l-1},0_l) + \rho^{(2)}(0_l,A_{l+1}) - \rho^{(2)}(A_l,0_{l+1}) - \rho^{(2)}(0_{l-1},A_l)],\\ &= \frac{P_m}{2}[C_{l-1}(1-C_l)F_{0,A}(l,l-1) + C_{l+1}(1-C_l)F_{0,A}(l,l+1)]\\ &\quad - \frac{P_m}{2}[C_l(1-C_{l-1})F_{A,0}(l,l-1) + C_l(1-C_{l+1})F_{A,0}(l,l+1)].\end{aligned} \tag{9}$$

Written in terms of the correlation functions, we can see that the right-hand side of Eq. (9) reflects the presence of correlations in the unbiased system. By setting $F_{\lambda,\mu}(l,m) \equiv 1$, we see that Eq. (9) relaxes directly to Eq. (1) which confirms that the simple mean-field model, given by Eqs. (1) and (2), amounts to ignoring correlation effects. This is the same as assuming that the occupancy status of lattice sites is independent.

To simplify the corrected mean-field equation, we substitute Eqs. (7) and (8) into Eq. (9) to find that all terms involving $F_{A,A}(l,m)$ cancel to give

$$\frac{\mathrm{d}\rho^{(1)}(A_l)}{\mathrm{d}t} = \frac{\mathrm{d}C_l}{\mathrm{d}t} = \frac{P_m}{2}[C_{l-1} - 2C_l + C_{l+1}]. \tag{10}$$

This confirms that the heuristic mean-field result given by Eq. (2) is indeed exact since correlation effects cancel. This means that, fortuitously, the approximate mean-field result (which relied on invoking the independence assumption) turns out to be exact and thereby provides a rigorous explanation of why several previous computational studies have indicated that density data extracted from an unbiased exclusion process model is exactly matched with the solution of a linear diffusion equation [8,9,11]. In Sec. III B we will show that this fortuitous cancellation of correlation functions does not always occur for other discrete mechanisms.

We will now explain, by means of an example, how the spatially dependent problems considered in this paper differ from our earlier work [14]. In our previous work we used

the same approach outlined here but limited our analysis to systems where the initial distribution of agents was spatially uniform. To demonstrate how the spatially uniform initial condition simplifies the analysis, we will briefly consider the unbiased motility mechanism in the case where the distribution of agents is spatially uniform so that $C_l = C$ for all lattice sites l. Under these conditions Eq. (9) becomes

$$\begin{aligned}\frac{\mathrm{d}\rho^{(1)}(A_l)}{\mathrm{d}t} &= \frac{P_m}{2}[\rho^{(2)}(A_{l-1},0_l) + \rho^{(2)}(0_l,A_{l+1}) \\ &\quad - \rho^{(2)}(A_l,0_{l+1}) - \rho^{(2)}(0_{l-1},A_l)], \\ &= \frac{P_m}{2}[\rho^{(2)}(A_l,0_{l+1}) + \rho^{(2)}(0_l,A_{l+1}) \\ &\quad - \rho^{(2)}(A_l,0_{l+1}) - \rho^{(2)}(0_l,A_{l+1})] \\ &= 0. \end{aligned} \tag{11}$$

Here we see that the mean-field description of the spatially uniform problem with unbiased motility states that the time rate of change of occupancy of any lattice site is zero. This major simplification arises because the terms in the evolution equation describing the motility process are independent of location because the agent distribution is uniform. This means that we have $\rho^{(2)}(A_{l-1},0_l) = \rho^{(2)}(A_l,0_{l+1})$ and $\rho^{(2)}(0_l,A_{l+1}) = \rho^{(2)}(0_{l-1},A_l)$. Given that our previous work only dealt with uniformly populated lattices, our previous analysis and computational algorithms were greatly simplified because of the cancellation of these spatial terms [14]. As they are documented, the corrected mean-field models reported in our previous study cannot be applied directly to spatially variable processes. The aim of the current paper is to use the same approach as the previous work, however we use this approach in a far more general framework enabling us to analyze and provide new insight into spatially variable processes. As a consequence of relaxing this major assumption, the corrected mean-field models and algorithms reported here are far more detailed than those considered in our previous work [14]. The benefit of dealing with this additional complexity is that the corrected mean-field models presented here provide us with new and important insight beyond what was demonstrated in our previous work.

B. Biased motility

We now consider the case where an isolated agent at site l attempts to step to sites $l \pm 1$ with unequal probability of $(1 \pm a)/2$. Here $|a| \leqslant 1$ is a bias parameter. Setting $a = 0$ means that there is no bias and the model relaxes to the unbiased motility model discussed in Sec. III A. Setting $a > 0$ means that an isolated agent is more likely to move to the right than the left, while setting $a < 0$ means that an isolated agent is more likely to move to the left than the right. The probability of motility per unit time is P_m, and attempted motility events that would place an agent on an occupied site are aborted. Incorporating this mechanism we can write down the evolution equation for $\rho^{(1)}(A_l)$ as follows:

$$\begin{aligned}\frac{\mathrm{d}\rho^{(1)}(A_l)}{\mathrm{d}t} &= \frac{P_m(1+a)}{2}[\rho^{(2)}(A_{l-1},0_l) - \rho^{(2)}(A_l,0_{l+1})] \\ &\quad + \frac{P_m(1-a)}{2}[\rho^{(2)}(0_l,A_{l+1}) - \rho^{(2)}(0_{l-1},A_l)].\end{aligned} \tag{12}$$

To make progress, we rewrite the right-hand side of Eq. (12) as the sum of two terms. The first term represents the unbiased component of the motility and the second term, which is proportional to a, represents the biased component of the motility. Expanding the $\rho^{(2)}$ terms into their correlation functions and rewriting all correlation functions in terms of $F_{A,A}(l,m)$ we obtain

$$\begin{aligned}\frac{\mathrm{d}\rho^{(1)}(A_l)}{\mathrm{d}t} = \frac{\mathrm{d}C_l}{\mathrm{d}t} &= \frac{P_m}{2}[C_{l-1} - 2C_l + C_{l+1}] \\ &\quad + a\frac{P_m}{2}[C_{l-1} - C_{l+1} + 2C_lC_{l+1}F_{A,A}(l,l+1) \\ &\quad - 2C_lC_{l-1}F_{A,A}(l,l-1)].\end{aligned} \tag{13}$$

Written in this form, we see that Eq. (13) reflects the effects of correlations in the bias terms, whereas there are no correlation effects in the unbiased component of motility. This is consistent with the results in Sec. III A since if we set $a = 0$ then the biased motility model reduces to the unbiased motility model which does not involve any correlation functions. In order to solve Eq. (13) we must now also develop a model that describes the evolution of the $F_{A,A}(l,l \pm 1)$ terms. This is achieved by writing down evolution equations for the appropriate $\rho^{(2)}$ terms. First we consider the evolution of $\rho^{(2)}(A_l,A_{l+1})$ given by

$$\begin{aligned}\frac{\mathrm{d}\rho^{(2)}(A_l,A_{l+1})}{\mathrm{d}t} &= \frac{P_m(1+a)}{2}[\rho^{(3)}(A_{l-1},0_l,A_{l+1}) \\ &\quad - \rho^{(3)}(A_l,A_{l+1},0_{l+2})] + \frac{P_m(1-a)}{2} \\ &\quad \times [\rho^{(3)}(A_l,0_{l+1},A_{l+2}) - \rho^{(3)}(0_{l-1},A_l,A_{l+1})].\end{aligned} \tag{14}$$

By rewriting Eq. (14) in terms of correlation functions and making use of the summation rule to reduce some of the $\rho^{(3)}$ terms into $\rho^{(2)}$ terms, it is possible to rewrite Eq. (14) in terms of an evolution equation for $F_{A,A}(l,l+1)$. The details of this algebraic manipulation, including the use of the KSA, are given in Appendix A2. The full evolution equation for $F_{A,A}(l,l+1)$ also depends on the values of $F_{A,A}(l,l+2)$ and we account for these terms by considering the evolution of $\rho^{(2)}(A_l,A_m)$ for $|l-m| > 1$, which can be expressed as

$$\begin{aligned}\frac{\mathrm{d}\rho^{(2)}(A_l,A_m)}{\mathrm{d}t} &= \frac{P_m(1+a)}{2}[\rho^{(3)}(A_{l-1},0_l,A_m) - \rho^{(3)}(A_l,0_{l+1},A_m)] + \frac{P_m(1+a)}{2}[\rho^{(3)}(A_l,A_{m-1},0_m) - \rho^{(3)}(A_l,A_m,0_{m+1})] \\ &\quad + \frac{P_m(1-a)}{2}[\rho^{(3)}(0_l,A_{l+1},A_m) - \rho^{(3)}(0_{l-1},A_l,A_m)] + \frac{P_m(1-a)}{2}[\rho^{(3)}(A_l,0_m,A_{m+1}) - \rho^{(3)}(A_l,0_{m-1},A_m)].\end{aligned} \tag{15}$$

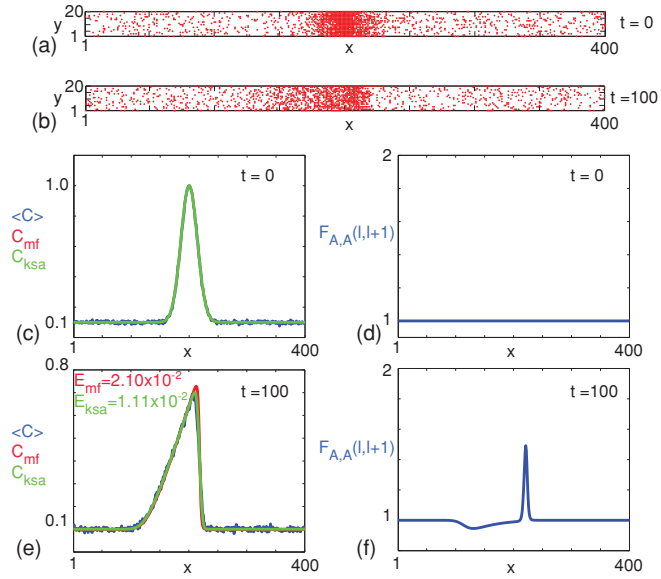

FIG. 2. (Color online) (a) and (b) show snapshots of 20 identically prepared realizations where the motility of agents is moderately biased with $P_m = \Delta = \tau = 1$ and $a = -0.5$. At $t = 0$ the initial occupancy of the lth lattice site was given by $C(l) = 0.1 + 0.9\exp\left[-(l-200)^2/400\right]$. Simulation results are shown at (a) $t = 0$ and (b) $t = 100$ where we see that the peak in density that was initially located at $x = 200$ has moved in the negative x direction owing to the motility bias. Results in (c) and (d) characterize the system at $t = 0$ with the average agent density (blue, medium gray), mean-field (red, dark gray), and corrected KSA mean-field (green, light gray) shown in (c) and the initial value of $F_{A,A}(l,l+1)$ given in (d). Results in (e) and (f) characterize the system at $t = 100$ with the average agent density (blue, medium gray), mean-field (red, dark gray), and corrected KSA mean-field (green, light gray) shown in (e) and the corresponding profile of $F_{A,A}(l,l+1)$ in (f). The RMSE for the mean-field and the corrected mean-field profiles are given as an inset in (e).

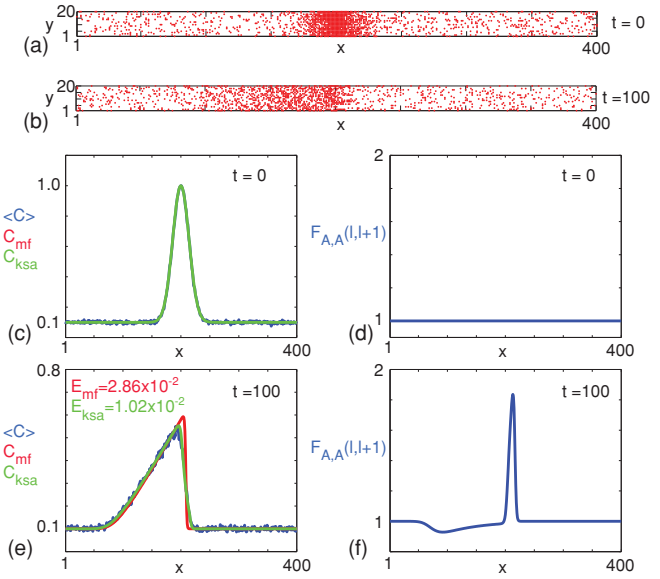

FIG. 3. (Color online) (a) and (b) show snapshots of 20 identically prepared realizations where the motility of agents is strongly biased with $P_m = \Delta = \tau = 1$ and $a = -1$. At $t = 0$ the initial occupancy of the lth lattice site was given by $C(l) = 0.1 + 0.9\exp\left[-(l-200)^2/400\right]$. Simulation results are shown at (a) $t = 0$ and (b) $t = 100$ where we see that the peak in density that was initially located at $x = 200$ has moved in the negative x direction owing to the motility bias. Results in (c) and (d) characterize the system at $t = 0$ with the average agent density (blue, medium gray), mean-field (red, dark gray), and corrected KSA mean-field (green, light gray) shown in (c) and the initial value of $F_{A,A}(l,l+1)$ given in (d). Results in (e) and (f) characterize the system at $t = 100$ with the average agent density (blue, medium gray), mean-field (red, dark gray), and corrected KSA mean-field (green, light gray) shown in (e) and the corresponding profile of $F_{A,A}(l,l+1)$ in (f). The RMSE for the mean-field and the corrected mean-field profiles are given as an inset in (e).

By writing all the $\rho^{(2)}$ terms in terms of the correlation functions and invoking the summation rule, we can express Eq. (15) in terms of an evolution equation for $F_{A,A}(l,m)$ for $|l-m| > 1$. The details of this algebraic manipulation and resulting equations are shown in Appendix A2.

1. Numerical results

The corrected mean-field model can now be solved and the solution compared with averaged simulation data. To achieve this we generated simulation data shown in Figs. 2(a) and 2(b) for $a = -0.5$ and Figs. 3(a) and 3(b) for $a = -1.0$.

(a) Discrete simulations. Simulations were performed on a one-dimensional lattice with $1 \leqslant l \leqslant 400$ and periodic boundary conditions imposed at $l = 1$ and $l = 400$. A random sequential update method, described elsewhere [8,9], was used to generate the simulation data using a standard intrinsic random number generator. Many identically prepared realizations were considered and in each case the lth lattice site was initially occupied with probability

$$C(l) = 0.1 + 0.9\exp\left[\frac{-(l-200)^2}{400}\right], \qquad (16)$$

giving, on average, a Gaussian-shaped initial profile of agents in each realization. Two sets of simulations were performed. The first set of simulations was for a moderately left-biased motility mechanism with $a = -0.5$, and the second set of simulations were performed with maximally left-biased motility by setting $a = -1$. To visualise the simulation data we present 20 realizations of the model in the 20 rows of the lattice shown in Figs. 2(a) and 2(b) for $a = -0.5$, and in Figs. 3(a) and 3(b) for $a = -1.0$. The snapshots in each row of Figs. 2(a), 2(b), 3(a), and 3(b) are independent realizations of the same stochastic process. Presenting these snapshots side-by-side conveniently illustrates the stochastic nature of the algorithm since the distribution of agents in each row can be quite different. To quantify the density profiles we average the occupancy of each corresponding lattice site using 400 identically prepared realizations to give a reliable estimate of C_l for $1 \leqslant l \leqslant 400$. These realizations are equivalent to the results shown in Figs. 2(a), 2(b), 3(a), and 3(b) except we considered 400 rows instead of 20. The averaged density profiles extracted from these 400 realizations are presented in Figs. 2(c) and 2(e) at $t = 0$ and $t = 100$, respectively, for $a - 0.5$. Equivalent results for $a = -1.0$ are shown in Figs. 3(c) and 3(e) at $t = 0$ and $t = 100$, respectively.

We will now make a brief comment about choosing to present averaged simulation data based on 400 identically prepared realizations. This choice was made to balance two competing interests. Had we chosen to present averaged density profiles constructed from a smaller number of identically prepared realizations, these profiles would have contained large fluctuations and it would have been difficult to visually interpret the meaning of these density profiles [12]. Alternatively, we could have presented averaged density profiles constructed from a much larger number of identically prepared realizations and these profiles would have contained very small fluctuations leading to very smooth profiles [12]. We chose to use 400 identically prepared realizations as a balance between these two competing effects. We wish to present profiles that contain relatively small fluctuations so that they represent a reliable approximation to the true average distribution, however we still wish to maintain sufficient fluctuations that the visual appearance of the profiles makes it clear that they are stochastic.

(b) Mean-field model. To compare the simulation data with the mean-field model we also solve a simplified version of Eq. (13) obtained by setting $F_{A,A}(l,\pm 1)\equiv 1$:

$$\frac{dC_l}{dt}=\frac{P_m}{2}[C_{l-1}-2C_l+C_{l+1}]+a\frac{P_m}{2}[C_{l-1}-C_{l+1}+2C_lC_{l+1}-2C_lC_{l-1}], \quad (17)$$

which is a semidiscrete equation comprising of a diffusive term describing the unbiased component of the motility and a nonlinear term describing the biased component of the motility. The solution of the mean-field model is obtained numerically (Appendix A4) for the same initial condition and boundary conditions used in the stochastic simulations. The resulting profiles are superimposed in Figs. 2(c) and 2(e) at $t=0$ and $t=100$, respectively, for $a=-0.5$, and in Figs. 3(c) and 3(e) at $t=0$ and $t=100$, respectively, for $a=-1.0$. We observe that the mean-field profile captures the main features of the simulation data with the exception that the mean-field profile overpredicts the peak density and the sharpness of the profile at $t=100$. Comparing the profiles in Figs. 2(e) and 3(e) we see the effect of changing the bias parameter since the peak profile moves further in the negative x direction as a is reduced. We will now make a quantitative comparison between the mean-field results and the simulation data. Throughout this manuscript we will make use of the root mean square error (RMSE) to quantify the match between density profiles constructed from simulation data and certain mean-field results. For the context of our work the RMSE can be written as

$$E=\sqrt{\frac{\sum_{l=1}^{l=N}(\langle C_l\rangle-\mathrm{MF}_l)^2}{N}}, \quad (18)$$

where N is the number of lattice sites used to compare the profiles, $\langle C_l\rangle$ is the average density of the lth lattice site constructed from the simulation data, and MF_l is the density of the lth lattice site predicted by some mean-field approximation. In our work MF_l will correspond to either the traditional mean-field model or the corrected mean-field model. The RMSE for the mean-field result profiles in Fig. 2(e) is $E=2.10\times 10^{-2}$, whereas the RMSE for the mean-field result profiles in Fig. 3(e) is $E=2.86\times 10^{-2}$. This difference in the RMSE indicates that the traditional mean-field result is less satisfactory as the amount of bias increases.

(c) Corrected mean-field model. We now solve the system of correlation equations to obtain an improved mean-field result which provides insight into the significance of making the independence assumptions that lead to the traditional mean-field model for biased motility. To achieve this we solve Eqs. (13)–(15) and obtain C_l, $F_{A,A}(l,l+1)$ and $F_{A,A}(l,m)$ for $m=l+2,l+3,l+4,\ldots$. While is it possible, in principle, to solve for $F_{A,A}(l,m)$ for all values of m to cover the periodic domain, it is more practical and computationally tractable to solve a truncated system $F_{A,A}(l,m)$ for $m=l+1,l+2,l+3,\ldots,l+M$ with the assumption that $F_{A,A}(l,l+M+1)\equiv 1$ [14]. To determine an appropriate value of M we solved the system iteratively for increasing values of M and examined how the distributions of C_l and $F_{A,A}(l,m)$ converged as M increased. Results presented in Figs. 2(c)–2(f) for $a=-0.5$, and in Figs. 3(c)–3(f) for $a=-1.0$ both correspond to $M=5$. We found that solving the systems of equations for larger values of M produced results that were visually indistinguishable from those in Figs. 2(c)–2(f) and Figs. 3(c)–3(f).

Comparing the corrected mean-field profile with the simulation data shows that the corrected mean-field model faithfully captures all the details of the simulation data. Unlike the traditional mean-field model, the corrected mean-field model predicts both the peak density and the shape of the simulation data accurately. Comparing the corrected mean-field profile and the simulation data in Figs. 2(e) and 3(e) shows that the RMSE for the corrected profile is less than the RMSE for the traditional mean-field result illustrating that the corrected mean-field model provides a better match to the simulation data. In addition to producing a corrected distribution for C_l, the solution of the corrected system also provides us with profiles of $F_{A,A}(l,m)$ for $m=l+1,l+2,l+3,l+4,l+5$. The distribution of $F_{A,A}(l,l+1)$ is shown in Figs. 2(d) and 2(f) for $a=-0.5$ and in Figs. 3(d) and 3(f) for $a=-1.0$. These profiles give us a quantitative measure of the importance of the correlations between occupancies of lattice sites. At $t=0$ we have $F_{A,A}(l,l+1)=1$ at all lattice sites since the average occupancies of all sites are independent of the average occupancies of the neighboring sites. By $t=100$ we see that $F_{A,A}(l,l+1)$ has evolved so that $F_{A,A}(l,l+1)\neq 1$ in certain locations on the lattice. For example, the large spike in $F_{A,A}(l,l+1)$ at $t=100$ occurs in the same location as the sharp change in C_l indicating that the occupancy status of lattice sites in this region are not independent. This explains why the solution of the corrected model is identical to the standard mean-field result in some areas of the lattice [where $F_{A,A}(l,m)=1$], whereas the density predicted by the corrected model is different to the density predicted by the standard mean-field result in other areas of the lattice [where $F_{A,A}(l,m)\neq 1$]. Comparing the profiles of $F_{A,A}(l,l+1)$ in Figs. 2(f) and 3(f) show that the maximum value of $F_{A,A}(l,l+1)$ is approximately 1.50 for $a=-0.5$ while the maximum value of $F_{A,A}(l,l+1)$ is approximately 1.85 for $a=-1.0$. This confirms that the correlation effects

are more pronounced as the motion becomes increasingly biased.

Although the corrected mean-field model for the biased motility problem provides an improved match to the simulation data compared to the traditional mean-field result, it is true that the discrepancy between the traditional mean-field result and the simulation data in Figs. 2 and 3 is relatively small. We will now consider the effects of agent proliferation and agent death and show that large deviations between the simulation data and the traditional mean-field model can result in this case.

C. Unbiased motility with agent proliferation and agent death

For this model we implement an unbiased agent motility mechanism where, during a motility event, an isolated agent at site l attempts to step to sites $l \pm 1$ with equal probability of $1/2$. The probability of motility per unit time is P_m and attempted motility events that would place an agent on an occupied site are aborted. To incorporate proliferation, an agent at site l is given the opportunity to proliferate, with proliferation events taking place at rate P_p per unit time. If successful, the daughter agent is placed at sites $l \pm 1$ with equal probability $1/2$. Potential proliferation events that would place a daughter agent on an occupied site are aborted. To incorporate death, an agent at site l is removed at rate P_d per unit time. Combining these three mechanisms we can write down the evolution equation for $\rho^{(1)}(A_l)$ as follows:

$$\frac{\mathrm{d}\rho^{(1)}(A_l)}{\mathrm{d}t} = \frac{P_m}{2}[\rho^{(2)}(A_{l-1},0_l) + \rho^{(2)}(0_l,A_{l+1}) - \rho^{(2)}(A_l,0_{l+1}) - \rho^{(2)}(0_{l-1},A_l)] + \frac{P_p}{2}[\rho^{(2)}(A_{l-1},0_l) + \rho^{(2)}(0_l,A_{l+1})] - P_d\rho^{(1)}(A_l). \tag{19}$$

Rewriting the system in terms of the correlation functions we obtain

$$\frac{\mathrm{d}\rho^{(1)}(A_l)}{\mathrm{d}t} = \frac{\mathrm{d}C_l}{\mathrm{d}t} = \frac{P_m}{2}[C_{l-1} - 2C_l + C_{l+1}] - P_dC_l + \frac{P_p}{2}\{C_{l-1}[1 - C_lF_{A,A}(l,l-1)] + C_{l+1}[1 - C_lF_{A,A}(l,l+1)]\}. \tag{20}$$

Here we see that the unbiased motility component and the agent death component do not engender any correlation effects directly since there are no correlation functions appearing in the evolution of the $\rho^{(1)}$ equation associated with these mechanisms. The correlation effects appear through the proliferation terms and so we need to develop evolution equations for the $\rho^{(2)}$ distributions. For nearest neighbor terms we obtain

$$\frac{\mathrm{d}\rho^{(2)}(A_l,A_{l+1})}{\mathrm{d}t} = \frac{P_m}{2}[\rho^{(3)}(A_{l-1},0_l,A_{l+1}) - \rho^{(3)}(0_{l-1},A_l,A_{l+1})] + \frac{P_m}{2}[\rho^{(3)}(A_l,0_{l+1},A_{l+2}) - \rho^{(3)}(A_l,A_{l+1},0_{l+2})] + \frac{P_p}{2}[\rho^{(3)}(A_{l-1},0_l,A_{l+1}) + \rho^{(3)}(A_l,0_{l+1},A_{l+2})] - 2P_d\rho^{(2)}(A_l,A_{l+1}). \tag{21}$$

For arbitrarily spaced lattice sites, with $|l-m| > 1$, we obtain

$$\frac{\mathrm{d}\rho^{(2)}(A_l,A_m)}{\mathrm{d}t} = \frac{P_m}{2}[\rho^{(3)}(A_{l-1},0_l,A_m) + \rho^{(3)}(A_l,A_{m-1},0_m) - \rho^{(3)}(A_l,0_{l+1},A_m) - \rho^{(3)}(A_l,A_m,0_{m+1})] + \frac{P_m}{2}[\rho^{(3)}(0_l,A_{l+1},A_m) + \rho^{(3)}(A_l,0_m,A_{m+1}) - \rho^{(3)}(0_{l-1},A_l,A_m) - \rho^{(3)}(A_l,0_{m-1},A_m)] + \frac{P_p}{2}[\rho^{(3)}(A_{l-1},0_l,A_m) + \rho^{(3)}(0_l,A_{l+1},A_m) + \rho^{(3)}(A_l,0_m,A_{m+1}) + \rho^{(3)}(A_l,0_m,A_{m-1})] - 2P_d\rho^{(2)}(A_l,A_m). \tag{22}$$

1. *Numerical results*

We are now in a position to solve the corrected mean-field model and compare the solution with averaged simulation data. To achieve this we generated four sets of simulation data shown in Figs. 4(a)–4(c) through 7(a)–7(c).

(a) Discrete model. Simulations were performed on a one-dimensional lattice with $1 \leqslant l \leqslant 200$, where in each realization the lth lattice site was initially occupied with probability

$$C(l) = 0.1 + 0.9\exp\left[\frac{-(l-100)^2}{400}\right], \tag{23}$$

and periodic boundary conditions were imposed at $l = 1$ and $l = 200$. At first we considered two proliferation-only cases. Both proliferation-only cases correspond to $P_m = 1.0$ and $P_d = 0.0$. The first proliferation-only case involved a relatively slow proliferation rate ($P_p = 0.0025$, Fig. 4) while the second proliferation-only case involved a relatively fast proliferation rate ($P_p = 0.025$, Fig. 5). To visualise the simulation data we present 20 realizations of the model in Figs. 4(a)–4(c) at $t = 0$, 1000, 2000, respectively, and in Figs. 5(a)–5(c) at $t = 0$, 100, 200, respectively. To quantify the density profiles we averaged the occupancy of each lattice site using 400 identically prepared realizations to give reliable estimates of C_l for $1 \leqslant l \leqslant 200$. These profiles are presented in Figs. 4(d), 4(f), and 4(h) at $t = 0$, 1000, 2000, respectively, and in Figs. 5(d), 5(f), and 5(h) at $t = 0$, 100, 200, respectively. During the simulations we see the effect of agent proliferation as the lattice sites become uniformly occupied so that the entire lattice is almost completely occupied by end of the simulation periods shown in Figs. 4 and 5.

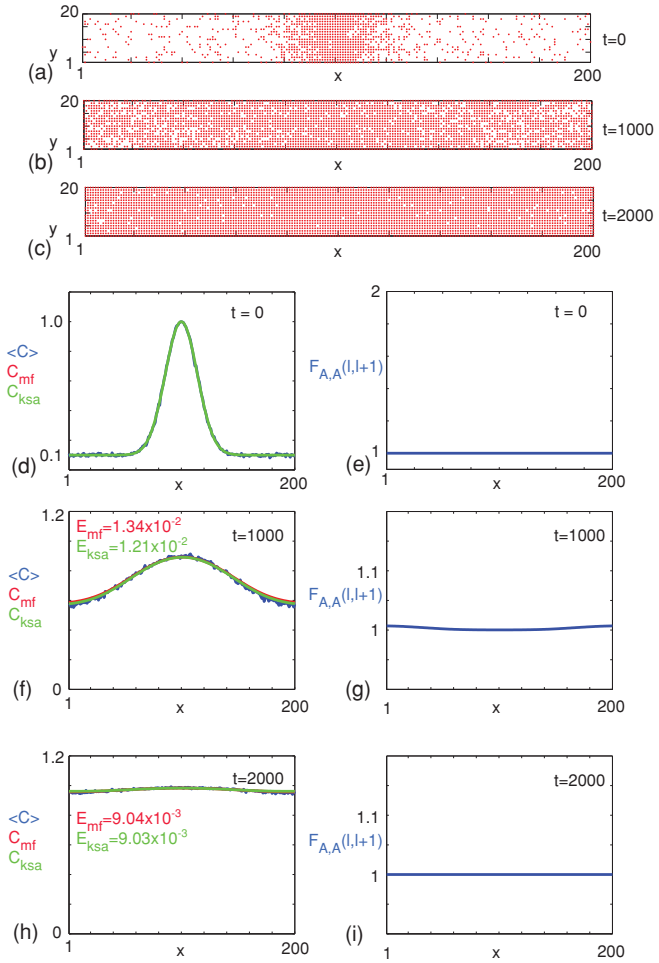

FIG. 4. (Color online) (a)–(c) show snapshots of 20 identically prepared realizations where the motility of agents is unbiased with $P_m = \Delta = \tau = 1$, and agents proliferate with a relatively slow proliferate rate, $P_p = 0.0025$, and no agent death, $P_d = 0$. At $t = 0$ the initial occupancy of the lth lattice site was given by $C(l) = 0.1 + 0.9\exp\left[-(l-100)^2/400\right]$. Simulation results are shown at (a) $t = 0$, (b) $t = 1000$, and (c) $t = 2000$ where we can see that the peak in density that was initially located at $x = 100$ becomes indistinguishable from the surrounding region of the lattice as t increases. Results in (d) and (e), (f) and (g), and (h) and (i) characterize the system at $t = 0$, $t = 1000$, and $t = 2000$, respectively. In each case the average agent density (blue, medium gray), mean-field (red, dark gray), and corrected KSA mean-field (green, light gray) are shown together, and the corresponding profiles of $F_{A,A}(l,l+1)$ are shown separately as indicated. The RMSE for the mean-field and corrected mean-field profiles are given as an inset in (f) and (h).

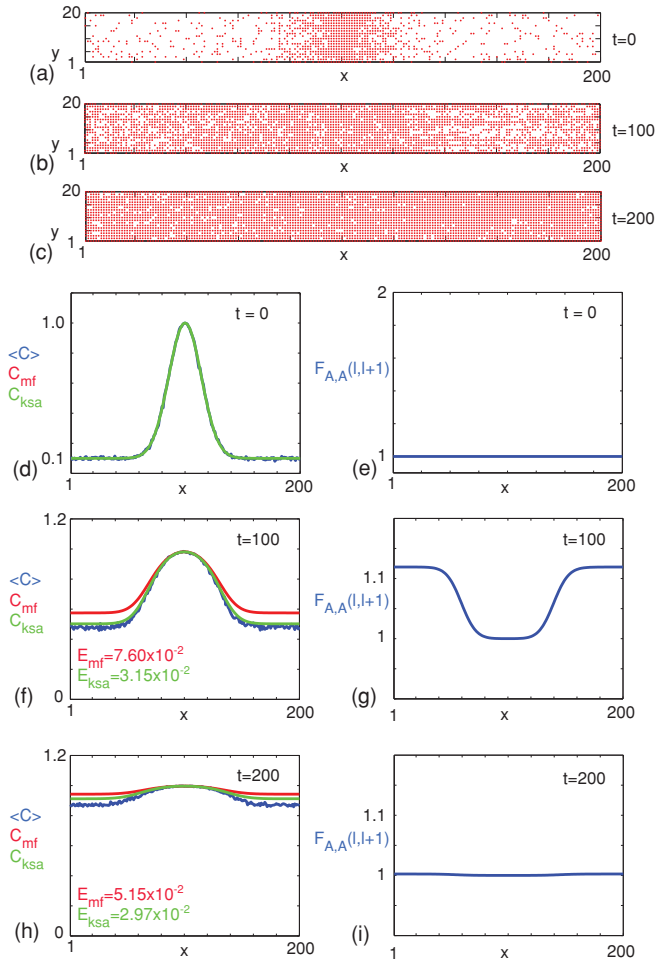

FIG. 5. (Color online) (a)–(c) show snapshots of 20 identically prepared realizations where the motility of agents is unbiased with $P_m = \Delta = \tau = 1$, and agents proliferate with a relatively faster proliferation rate, $P_p = 0.025$, and no agent death, $P_d = 0$. At $t = 0$ the initial occupancy of the lth lattice site was given by $C(l) = 0.1 + 0.9\exp\left[-(l-100)^2/400\right]$. Simulation results are shown at (a) $t = 0$, (b) $t = 100$, and (c) $t = 200$ where we can see that the peak in density that was initially located at $x = 100$ becomes indistinguishable from the surrounding region of the lattice as t increases. Results in (d) and (e), (f) and (g), and (h) and (i) characterize the system at $t = 0$, $t = 100$, and $t = 200$, respectively. In each case the average agent density (blue, medium gray), mean-field (red, dark gray), and corrected KSA mean-field (green, light gray) are shown together, and the corresponding profiles of $F_{A,A}(l,l+1)$ are shown separately as indicated. The RMSE for the mean-field and corrected mean-field profiles are given as an inset in (f) and (h).

(b) Mean-field model. To compare the simulation data with a mean-field model we also solve a simplified version of Eq. (20) obtained by setting $F_{A,A}(l, \pm 1) \equiv 1$:

$$\frac{dC_l}{dt} = \frac{P_m}{2}[C_{l-1} - 2C_l + C_{l+1}] + \frac{P_p}{2}[C_{l-1}(1-C_l) + C_{l+1}(1-C_l)] - P_d C_l. \quad (24)$$

This semidiscrete equation reflects linear diffusion, with births and deaths as "reaction" terms. The solution of the mean-field model is obtained numerically (Appendix A4) for the same initial condition and boundary conditions used in the stochastic simulations and the resulting profiles are superimposed in Figs. 4(d), 4(f), 4(h), 5(d), 5(f), and 5(h). In the case of the relatively small proliferation rate ($P_p = 0.0025$, Fig. 4) we observe that the traditional mean-field result captures the density profiles accurately, however for the larger proliferation rate ($P_p = 0.025$, Fig. 5) we observe a large deviation between the simulation data and the mean-field model, particularly at $t = 100$ where the mean-field result completely fails to capture the density profile away from the central part of the lattice.

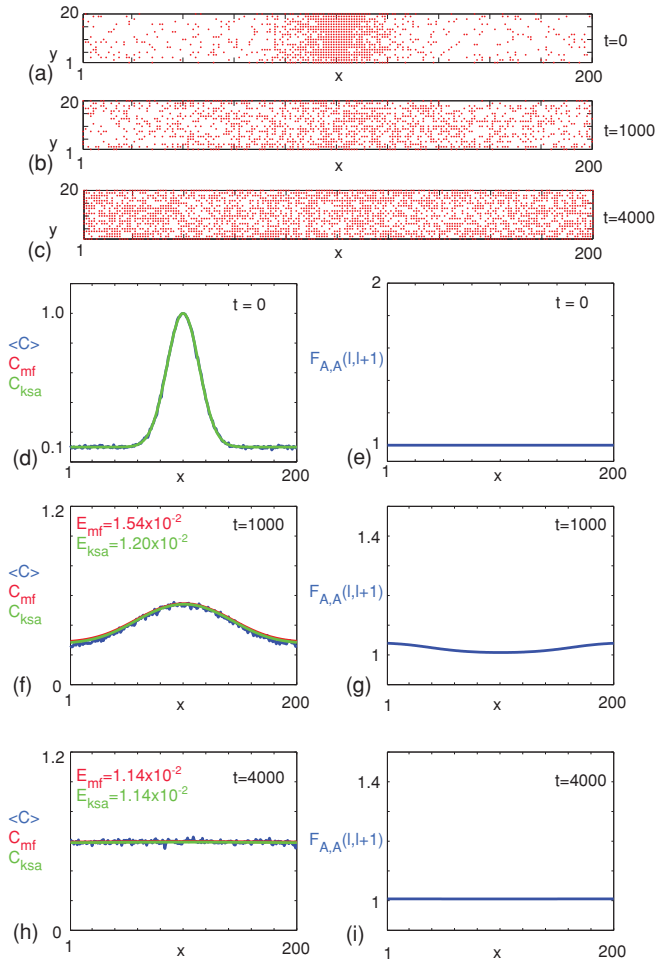

FIG. 6. (Color online) (a)–(c) show snapshots of 20 identically prepared realizations where the motility of agents is unbiased with $P_m = \Delta = \tau = 1$, and agents proliferate and die with relatively slow proliferation and death rates, $P_p = 0.0025$ and $P_d = 0.001$. At $t = 0$ the initial occupancy of the lth lattice site was given by $C(l) = 0.1 + 0.9\exp\left[-(l-100)^2/400\right]$. Simulation results are shown after (a) $t = 0$, (b) $t = 1000$, and (c) $t = 4000$ where we can see that the peak in density that was initially located at $x = 100$ becomes indistinguishable from the surrounding region of the lattice. As t increases we see that the system tends toward a spatially uniform steady state where the agent density is less than confluence. Results in (d) and (e), (f) and (g), and (h) and (i) characterizse the system at $t = 0, t = 1000$, and $t = 4000$, respectively. In each case the average agent density (blue, medium gray), mean-field (red, dark gray), and corrected KSA mean-field (green, light gray) are shown together, and the corresponding profiles of $F_{A,A}(l,l+1)$ are shown separately as indicated. The RMSE for the mean-field and corrected mean-field profiles are given as an inset in (f) and (h).

(c) Corrected mean-field model. To obtain the corrected mean-field result we solve Eqs. (19)–(22) and obtain C_l, $F_{A,A}(l,m)$ for $m = l+1, l+2, l+3, l+4, \ldots, l+M$. As for the biased motility case we determined the value of M iteratively and found that setting $M = 10$ was sufficient to obtain the converged results given in Figs. 4(d)–4(i) and Figs. 5(d)–5(i). Comparing the profiles for the relatively small proliferation rate ($P_p = 0.0025$, Fig. 4) shows that the traditional mean-field profile, the corrected mean-field profile, and the simulation results are visually indistinguishable. However, the profiles for the relatively large proliferation rate ($P_p = 0.025$, Fig. 5) show that the corrected mean-field model gives a significant improvement relative to the traditional mean-field profile as it accurately captures the details of the simulation data. This improvement is reflected in the RMSE data given in Fig. 5. Results in Figs. 4(e), 4(g), 4(i), 5(e), 5(g), and 5(i) show the distribution of $F_{A,A}(l,l+1)$ for the lower and higher proliferation rates, respectively. This data provides us with additional information about the effect of correlations in the system. In the small proliferation rate system we have $F_{A,A}(l,l+1) \approx 1$ at all locations on the lattice for all times considered. Alternatively for the high proliferation rate system we see that in the central part of the lattice we have $F_{A,A}(l,l+1) \approx 1$ and in this region there is virtually no difference between the corrected mean-field result and the traditional mean-field result. In regions of the lattice further away from the peak in density we see that $F_{A,A}(l,l+1) > 1$ and this corresponds to the region where there is a significant deviation between the traditional mean-field result and the corrected mean-field profile.

We now consider two further sets of simulation data where agents undergo both proliferation and death events. We choose to focus on two cases with $P_p > P_d$. In the first case we consider relatively slow proliferation and death rates with $P_p = 0.0025$ and $P_d = 0.001$ (Fig. 6) and in the second case we consider a system with a relatively faster proliferation and death rates with $P_p = 0.025$ and $P_d = 0.01$ (Fig. 7). Generally, for this choice of parameters, the population does not become extinct on the time scale of interest. The alternative case, where $P_d > P_p$, generally results in a trivial long-term steady state where there are no agents remaining on the lattice.

Results are presented in Figs. 6 and 7 in exactly the same way that results were presented in Figs. 4 and 5 except that we have incorporated agent death. Snapshots of simulation results in Figs. 6(a)–6(c) at $t = 0$, 1000, 4000, respectively, and in Figs. 7(a)–7(c) at $t = 0$, 100, 400, respectively, show that the number of agents present on the lattice increases with time but fails to fill the lattice completely, as observed in Figs. 4 and 5. Density profiles for the slow proliferation and death system in Figs. 6(d), 6(f), and 6(h) show that the traditional mean-field result is able to capture the simulation data adequately. Alternatively, equivalent data for the faster proliferation and death system in Figs. 7(d), 7(f), and 7(h) show that the traditional mean-field model fails to capture the details of the simulation density profiles and confirms that the corrected mean-field profile is able to describe these details accurately.

D. Approximately corrected mean-field models of invasion wave phenomena

For all of the models considered so far we have seen that the traditional mean-field result can either exactly predict the simulation results or there can be large deviations between the mean-field result and the simulation data. In all cases presented where there are deviations between the traditional mean-field result and the simulation data we observe that the corrected mean-field result is able to accurately capture the

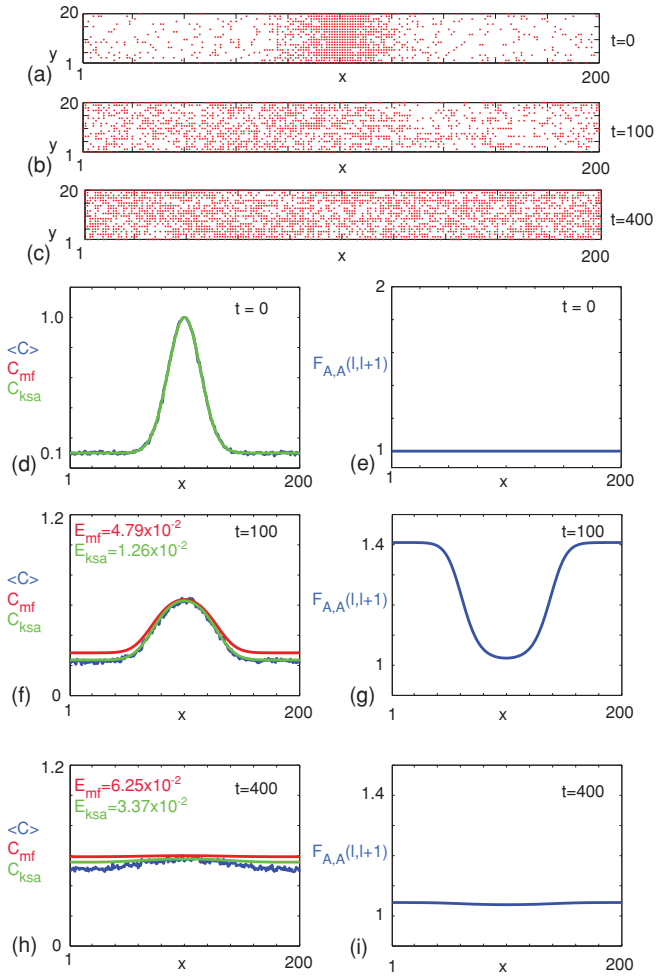

FIG. 7. (Color online) (a)–(c) show snapshots of 20 identically prepared realizations where the motility of agents is unbiased with $P_m = \Delta = \tau = 1$, and agents proliferate and die with relatively faster proliferation and death rates, $P_p = 0.025$ and $P_d = 0.01$. At $t = 0$ the initial occupancy of the lth lattice site was given by $C(l) = 0.1 + 0.9\exp\left[-(l-100)^2/400\right]$. Simulation results are shown after (a) $t = 0$, (b) $t = 100$, and (c) $t = 400$ where we can see that the peak in density that was initially located at $x = 100$ becomes indistinguishable from the surrounding region of the lattice. As t increases we see that the system tends toward a spatially uniform steady state where the agent density is less than confluence. Results in (d) and (e), (f) and (g), and (h) and (i) characterize the system at $t = 0$, $t = 100$, and $t = 400$, respectively. In each case the average agent density (blue, medium gray), mean-field (red, dark gray), and corrected KSA mean-field (green, light gray) are shown together, and the corresponding profiles of $F_{A,A}(l,l+1)$ are shown separately as indicated. The RMSE for the mean-field and corrected mean-field profiles are given as an inset in (f) and (h).

simulation data. This is a promising result. However, care must be taken to apply this approach in general. If we examine the evolution of the $F_{A,A}(l,m)$ equations in Appendix A3 we see that the differential equations governing the evolution of the correlation functions involve rational expressions with terms like C_l, $(1 - C_l)$ and $C_l(1 - C_l)$ appearing in the denominator. This implies that the correlation functions are unbounded when certain lattice sites are either completely occupied ($C_l = 1$) or

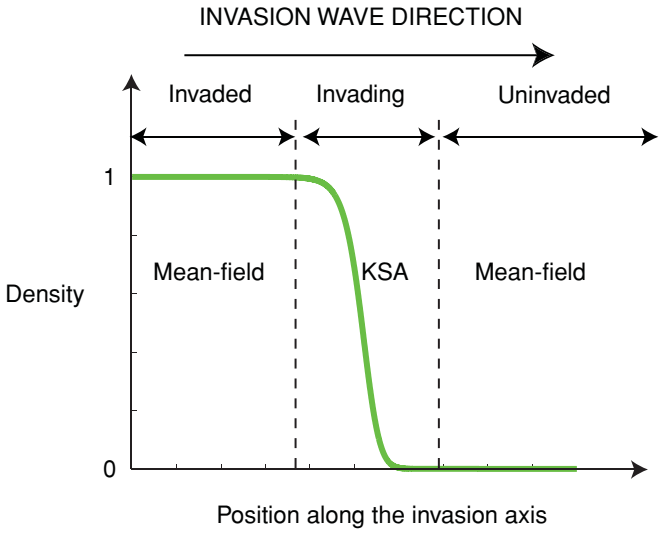

FIG. 8. (Color online) Schematic invasion wave profile with invading cell density profile shown in green (light gray) as it invades from left to right. The invaded, invading, and uninvaded regions are marked.

completely vacant ($C_l = 0$). This complication motivated us to use Gaussian-like initial profiles in Secs. III B–III C since these initial profiles avoided the complication that $C_l = 1$ and $C_l = 0$ at any site.

We will now focus on applying the corrected models to represent cell invasion processes like that schematically depicted in Fig. 8. We consider three regions relative to the leading edge of the wave, namely: (i) behind the wavefront where $C \approx 1$ (the invaded region); (ii) at the wavefront where $0 < C < 1$ (the invading region), and (iii) ahead of the wavefront where $C \approx 0$ (the uninvaded region). To simulate this kind of invasion system we repeat the simulations shown in Figs. 4 and 5 except we change the initial condition so that, in each realization, the lth lattice site was initially occupied with probability

$$C(l) = \begin{cases} 1, & 1 \leqslant l < 50\,, \\ 1 - \left[\frac{l-50}{50}\right], & 50 \leqslant l \leqslant 100\,, \\ 0, & 100 < l \leqslant 200\,. \end{cases} \tag{25}$$

This initial condition involves setting both $C_l = 1$ and $C_l = 0$ for certain lattice sites. For this initial condition we apply reflecting boundary conditions at $l = 1$ and $l = 200$. We now consider two sets of simulation data for $P_m = 1$ and $P_d = 0.0$ with the same initial condition given by Eq. (25). The first set of simulation data are for a relatively slow proliferation rate [$P_p = 0.005$, Figs. 9(a)–9(c)] and the second set of simulation data are for a relatively faster proliferation rate [$P_p = 0.05$, Figs. 10(a)–10(c)]. For both cases, snapshots in Figs. 9(a)–9(c) and 10(a)–10(c) show that the agents move and proliferate leading to the formation of an invasion wave which moves in the positive x direction. For the relatively slow proliferation rate the system forms a gently sloping invasion wave profile while the system with the higher proliferation rate forms a steeper invasion wave. Averaged density data from these simulations are presented in Figs. 9(d)–9(f) and 10(d)–10(f)

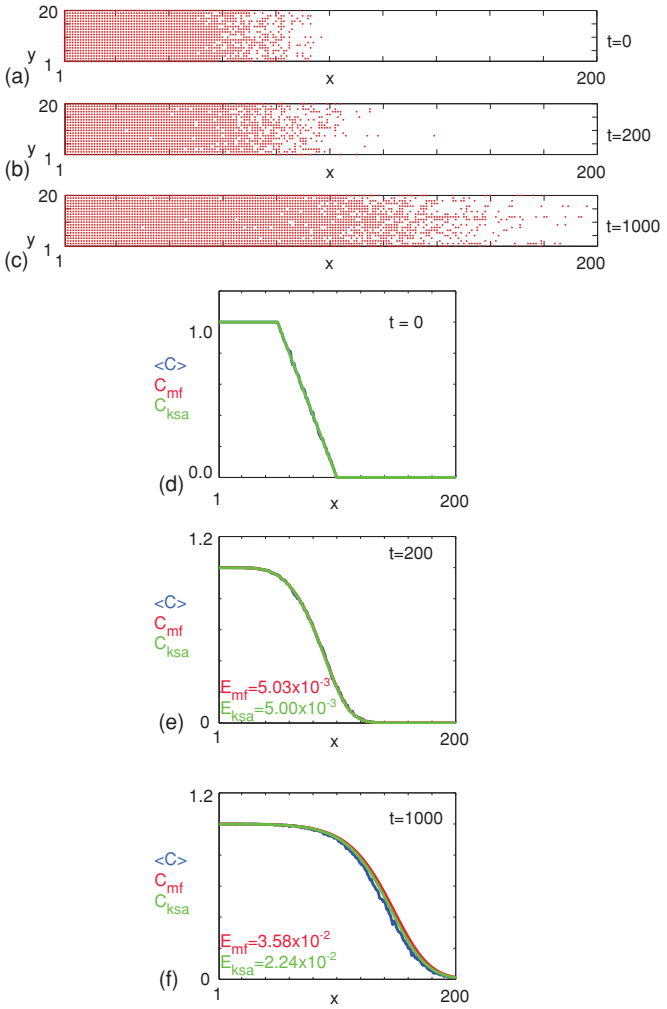

FIG. 9. (Color online) (a)–(c) show snapshots of 20 identically prepared realizations where the motility of agents is unbiased with $P_m = \Delta = \tau = 1$, and agents proliferate with a relatively slow proliferation rate, $P_p = 0.005$, and do not die, $P_d = 0$. At $t = 0$ the initial occupancy of the lth lattice site was given by Eq. (25). Simulation results are shown at (a) $t = 0$, (b) $t = 200$, and (c) $t = 1000$ indicating that the combined motility and proliferation of agents leads to the formation of an invasion wave which moves from left to right. Results in (d)–(f) characterize the system at $t = 0$, $t = 200$, and $t = 1000$, respectively. In each case the average agent density (blue, medium gray), mean-field (red, dark gray), and corrected KSA mean-field (green, light gray) are shown and we can see that there is a small deviation between the simulation data, the traditional mean-field result, and the corrected mean-field result. The corrected mean-field result is obtained using the procedure outlined in Sec. III D with $\epsilon = 1 \times 10^{-8}$. The RMSE for the mean-field and corrected mean-field profiles are given as an inset in (e) and (f).

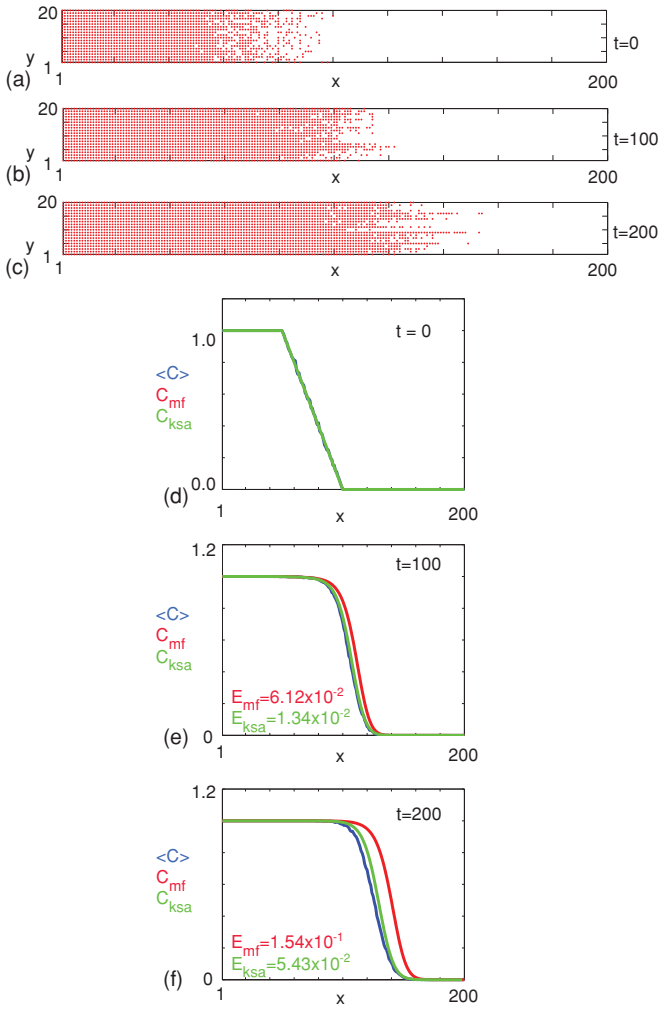

FIG. 10. (Color online) (a)–(c) show snapshots of 20 identically prepared realizations where the motility of agents is unbiased with $P_m = \Delta = \tau = 1$, and agents proliferate with a relatively fast proliferation rate, $P_p = 0.05$, and do not die, $P_d = 0$. At $t = 0$ the initial occupancy of the lth lattice site was given by Eq. (25). Simulation results are shown at (a) $t = 0$, (b) $t = 100$, and (c) $t = 200$ indicating that the combined motility and proliferation of agents leads to the formation of an invasion wave which moves from left to right. Results in (d)–(f) characterize the system at $t = 0$, $t = 100$, and $t = 200$, respectively. In each case the average agent density (blue, medium gray), mean-field (red, dark gray), and corrected KSA mean-field (green, light gray) are shown and we can see that there is a large deviation between the simulation data and the traditional mean-field result. The corrected mean-field result is obtained using the procedure outlined in Sec. III D with $\epsilon = 1 \times 10^{-8}$. The RMSE for the mean-field and corrected mean-field profiles are given as an inset in (e) and (f).

which shows how the initial ramp profile evolves into an invasion wave similar in shape to the schematic shown in Fig. 8. To compare the averaged simulation data with the mean-field model we set $F_{A,A}(l, \pm 1) \equiv 1$ in Eq. (20), as before, and solve the resulting system, Eq. (24). Results in Figs. 9(d)–9(f) show that the traditional mean-field model and the simulation data match reasonably well, whereas the results in Figs. 10(d)–10(f) show that there is a large deviation between the simulation data and the traditional mean-field model for the higher proliferation rate. In particular, we see that the simulation data is retarded relative to the mean field invasion wave [16] and by $t = 200$ there is a very large deviation between the simulation data and the traditional mean-field result.

To generate an improved mean-field result we must modify our previous approach for solving the correlation equations and to do this we use a hybrid method where we solve the truncated system of correlation equations in those regions of the lattice where $\epsilon < C < (1-\epsilon)$ and use the traditional mean-field model in the remaining regions of the lattice where $(1-\epsilon) \leqslant C \leqslant 1$ and $0 \leqslant C \leqslant \epsilon$. This hybrid method involves dividing the invasion wave profile shown schematically in Fig. 8 into the invaded, invading, and uninvaded regions. We apply the traditional mean-field model to solve for C_l in the invaded and uninvaded regions while we apply the corrected mean-field model to solve for C_l in the invading region. The accuracy of this approach depends on the value of ϵ that is chosen to delineate these regions, and also the level at which the correlation system is truncated for $F_{A,A}(l,m)$ with $m = l+1, l+2, l+3, l+4, \ldots, l+M$. To demonstrate the effectiveness of this strategy we present corrected mean-field results in Figs. 9(d)–9(f) and 10(d)–10(f) that were obtained by setting $\epsilon = 1 \times 10^{-8}$ and $M = 10$. As expected, for a relatively slow proliferation rate (Fig. 9), we see that the corrected mean-field result and the traditional mean-field result are very similar. Alternatively, the corrected mean-field result for the high proliferation rate (Fig. 10) provides a far better match to the simulation data than the traditional mean-field result. These differences are reflected in the RMSE data given in Figs. 9 and 10.

As we have mentioned, the accuracy of the corrected mean-field model depends on the choice of ϵ. Our results in Figs. 9 and 10 correspond to $\epsilon = 1 \times 10^{-8}$ and we found that reducing ϵ further did not change the corrected mean-field results in these cases. We did, however, test larger values of ϵ and found that larger values gave poorer results. This is an intuitive result since increasing ϵ means that we are increasing the size of the lattice where the traditional mean-field model is applied. In general, the relationship between the accuracy of the corrected mean-field model and the value of ϵ is complicated since it also depends on the shape of the density profile. This means that for invasion wave problems the accuracy of the hybrid method will depend both on ϵ and any other factor that influences the shape of the density profile such as the initial condition, the boundary conditions, and the parameters P_m and P_p. We have not investigated the details of the complicated relationship here since our aim is to demonstrate the application of the hybrid method. A detailed analysis of the accuracy of the hybrid method is left as an open question for future research.

Although it was necessary to use the hybrid approach to solve the corrected mean-field model for the invasion wave problems in Figs. 9 and 10, we remark that the hybrid method was not required to solve the problems described in Figs. 4 and 5 even though these previous problems involved the lattice becoming uniformly occupied to confluence toward the end of the simulation. In this previous case the system of correlation equations was applied everywhere across the domain and the numerical solution remained bounded for all times considered. This implies that the hybrid method is only required when we specify $C_l = 0$ or $C_l = 1$ at the beginning of the simulation like we did in Figs. 9 and 10. In the previous case (Figs. 4 and 5) the solution evolved in such a way that the governing equations did not blow up, implying that there was some cancellation effects that negated this issue.

E. Discussion and conclusion

Many mean-field models in the exclusion process literature are derived by invoking an independence assumption [6,8–11,13]. This assumption states that the average occupancy status of a lattice site is independent of the average occupancy status of other lattice sites. Given that most exclusion processes involve agent transitions to and from neighboring lattice sites, the independence assumption appears to be intuitively invalid [15]. However without any formal way of relaxing the independence assumption it seems probable that violating the independence assumption could explain why some mean-field models fail to match simulation data [8,9]. In this work we develop corrected mean-field descriptions of various exclusion-process-based models that include (i) unbiased motility, (ii) biased motility, and (iii) unbiased motility with birth and death processes. The corrected mean-field model describes the evolution of k-point distribution functions that represent the exclusion process without making any independence assumption. This procedure leads to an infinite system of coupled nonlinear equations which are truncated using a moment closure approximation. In this study we close the system using the KSA. Our results show that the simplest unbiased motility mechanism is governed by the same mean-field model that is obtained by invoking the independence assumption. This demonstrates that the independence assumption leads to an exact result by coincidence. For biased motility we show that small deviations between simulation data and standard mean-field models are corrected using the improved KSA mean-field model. For unbiased motility incorporating agent birth and death we show that large deviations between simulation data and standard mean-field models are reduced using the corrected KSA mean-field model. In summary, our analysis provides a rigorous explanation of why certain previous mean-field models based on the independence assumption appear to provide a good match to simulation data while other previous mean-field models fail to capture the details of the discrete simulation data. In these latter cases the corrected mean-field models presented here provide an improved match to simulation data.

A key contribution of our analysis is that we study problems where the initial agent density varies spatially across the lattice. This is a significant generalization of previous works that have been limited to studying initially uniform problems. These previous uniform studies have considered problems that have arisen in surface chemistry [17,18], ecology [5], and cell biology [14]. Our interest is to apply exclusion process models to represent cell biology phenomena, which includes the spreading of cell populations as well as invasion wave processes [21,22] that have broad applications to understanding wound healing, malignant invasion, and developmental biology. These problems are inherently spatially dependent since we are interested in predicting the evolution of moving fronts and previous studies based on initially uniform problems do not apply. The KSA-based corrected mean-field model is fully documented here and we show that the improved model involves solving a system of coupled nonlinear differential equations describing several correlation functions, $F_{A,A}(l,m)$.

These functions provide us with a quantitative measure of the correlation between the occupancy status of lattice sites l and m. In all cases the differential equations governing the evolution of the correlation functions involve rational expressions with terms like C_l, $(1-C_l)$ and/or $C_l(1-C_l)$ on the denominator. This implies that the correlation functions are unbounded when the probability of certain lattice sites are either completely occupied ($C_l = 1$) or completely vacant ($C_l = 0$).

The issue regarding the correlation functions becoming unbounded when certain lattice sites are either completely occupied or completely vacant never arose in previous studies focusing on initially uniform problems [5,14,17,18]. In these previous studies it made no sense to consider the evolution of a completely and uniformly occupied lattice or a completely and uniformly vacant lattice. In contrast, for the more general spatially variable problems considered here, we must deal with this complication. For demonstrative purposes, we present simulation data and solutions of the corrected mean-field model for a range of problems where the initial distribution of agents on the lattice is such that $0 < C_l < 1$ for all lattice sites across the lattice. Studying this kind of initial condition allowed us to demonstrate how the corrected mean-field model performed relative to the traditional mean-field model for a range of problems. We also present results for a more general cell invasion problem where the initial distribution of agents includes certain regions of the lattice that are completely occupied and certain regions of the lattice that are vacant. Here we adopt a hybrid approach to solve this problem by applying the corrected mean-field model to regions of the lattice with $\epsilon < C_l < (1-\epsilon)$, while using the traditional mean-field model elsewhere on the lattice. Our simulation data confirms that this hybrid approach leads to an improved mean-field solution that outperforms the traditional mean-field result.

Various extensions of this work are possible with obvious applications to exclusion process models on 2D and 3D lattices. We would also like to make the point that although this work is based on the traditional KSA closure scheme, it is possible to incorporate other closure schemes into the models outlined here. For example, previous investigators have indicated that the accuracy of the traditional KSA closure scheme can be improved by incorporating a power series [19,23,24] or exponential factor [5]. We have not used these correction methods in the present study since our simulation data demonstrates that the standard KSA closure scheme performs adequately for the problems considered here. We note, however, that any future developments in terms of new closure schemes or new corrections to the KSA closure scheme could, in principle, be incorporated into the models reported here.

APPENDIX: $\rho^{(2)}$ EVOLUTION EQUATIONS

1. Simplifying relations

To simplify the various evolution equations for $\rho^{(2)}(A_l, A_m)$ presented in the main part of the paper we make use of three results described briefly here.

a. Conservation rule

In all models we make use of a summation rule that allows us to collapse certain $\rho^{(3)}$ terms into $\rho^{(2)}$. The summation rule can be written as

$$\sum_{\sigma_n} \rho^{(3)}(\sigma_l,\sigma_m,\sigma_n) = \rho^{(2)}(\sigma_l,\sigma_m). \tag{A1}$$

For example,

$$\rho^{(3)}(A_l,A_m,A_{l+1}) + \rho^{(3)}(A_l,A_m,0_{l+1}) = \rho^{(2)}(A_l,A_m). \tag{A2}$$

b. Kirkwood superposition approximation

In all models except for the simple unbiased motility case, some of the $\rho^{(3)}$ terms cannot be reduced using the summation rule. In this case we close the system approximately by introducing an approximate relationship between the $\rho^{(3)}$ and $\rho^{(2)}$ distribution functions known as the KSA which can be written as

$$\begin{aligned}\rho^{(3)}(A_l,A_m,A_s) &= \frac{\rho^{(2)}(A_l,A_m)\rho^{(2)}(A_l,A_s)\rho^{(2)}(A_m,A_s)}{\rho^{(1)}(A_l)\rho^{(1)}(A_m)\rho^{(1)}(A_s)} \\ &= C_l C_m C_s F_{A,A}(l,m)F_{A,A}(l,s)F_{A,A}(m,s).\end{aligned} \tag{A3}$$

This approximation has been widely studied [5,14,17–20], and as evidenced by our computational results in the main paper, the KSA proves to be a sufficiently accurate closure scheme.

c. Correlation functions

We also make use of the relationship between the $\rho^{(2)}$ distribution functions and the correlation functions together with the product rule of differentiation to simplify the temporal terms:

$$\begin{aligned}\frac{\mathrm{d}\rho^{(2)}(A_l,A_m)}{\mathrm{d}t} &= \frac{\mathrm{d}[C_l C_m F_{A,A}(l,m)]}{\mathrm{d}t} = C_l C_m \frac{\mathrm{d}F_{A,A}(l,m)}{\mathrm{d}t} \\ &\quad + F_{A,A}(l,m)\left[C_m \frac{\mathrm{d}C_l}{\mathrm{d}t} + C_l \frac{\mathrm{d}C_m}{\mathrm{d}t}\right].\end{aligned} \tag{A4}$$

Using these three relationships we now present the final equations governing the evolution of the correlation functions for various mechanisms explored in this study. We only present the final versions of these equations. These final versions have been derived making use of the summation rule and the KSA where appropriate. For convenience we will prime notation F' to represent temporal derivatives $F'_{A,A}(l,m) = \mathrm{d}F_{A,A}(l,m)/\mathrm{d}t$. In this Appendix all correlation functions will refer to the correlation between two occupied sites $F_{A,A}(l,m)$ and we will drop the subscript for convenience so that $F(l,m) = F_{A,A}(l,m)$.

2. Biased motility

The evolution of $F(l,l+1)$ is given by

$$\begin{aligned}F'(l,l+1) = &-F(l,l+1)\left[\frac{C'_{l+1}}{C_{l+1}}+\frac{C'_l}{C_l}\right]\\ &+\frac{P_m}{2}\left[\frac{C_{l-1}}{C_l}F(l-1,l+1)+\frac{C_{l+2}}{C_{l+1}}F(l,l+2)-2F(l,l+1)\right]\\ &+\frac{P_m a}{2}\left\{\frac{C_{l-1}}{C_l(1-C_l)}[1-C_lF(l,l-1)][1-C_lF(l,l+1)]F(l-1,l+1)\right.\\ &+\frac{1}{(1-C_{l-1})}[1-C_{l-1}F(l,l-1)][1-C_{l-1}F(l-1,l+1)]F(l,l+1)\\ &-\frac{1}{(1-C_{l+2})}[1-C_{l+2}F(l,l+2)][1-C_{l+2}F(l+1,l+2)]F(l,l+1)\\ &\left.-\frac{C_{l+2}}{C_{l+1}(1-C_{l+1})}[1-C_{l+1}F(l,l+1)][1-C_{l+1}F(l+1,l+2)]F(l,l+2)\right\}. \end{aligned}\tag{A5}$$

For any general distance $F(l,m)$, where $|l-m|>1$, we obtain

$$\begin{aligned}F'(l,m) = &-F(l,m)\left[\frac{C'_l}{C_l}+\frac{C'_m}{C_m}\right]+\frac{P_m}{2}\left[\frac{C_{l-1}}{C_l}F(l-1,m)+\frac{C_{l+1}}{C_l}F(l+1,m)\right.\\ &\left.+\frac{C_{m-1}}{C_m}F(l,m-1)+\frac{C_{m+1}}{C_m}F_{A,A}(l,m+1)-4F(l,m)\right]\\ &+\frac{P_m a}{2}\left\{\frac{C_{l-1}}{C_l(1-C_l)}[1-C_lF(l,m)][1-C_lF(l,l-1)]F(l-1,m)\right.\\ &+\frac{C_{m-1}}{C_m(1-C_m)}[1-C_mF(l,m)][1-C_mF(m,m-1)]F(l,m-1)\\ &+\frac{1}{(1-C_{l-1})}[1-C_{l-1}F(l,l-1)][1-C_{l-1}F(l-1,m)]F(l,m)\\ &+\frac{1}{(1-C_{m-1})}[1-C_{m-1}F(l,m-1)][1-C_{m-1}F(m,m-1)]F(l,m)\\ &-\frac{1}{(1-C_{l+1})}[1-C_{l+1}F(l,l+1)][1-C_{l+1}F(l+1,m)]F(l,m)\\ &-\frac{1}{(1-C_{m+1})}[1-C_{m+1}F(m,m+1)][1-C_{m+1}F(l,m+1)]F(l,m)\\ &-\frac{C_{l+1}}{C_l(1-C_l)}[1-C_lF(l,l+1)][1-C_lF(l,m)]F(l+1,m)\\ &\left.-\frac{C_{m+1}}{C_m(1-C_m)}[1-C_mF(l,m)][1-C_mF(m,m+1)]F(l,m+1)\right\}. \end{aligned}\tag{A6}$$

3. Unbiased motility with agent proliferation and agent death

The evolution of $F(l,l+1)$ is given by

$$\begin{aligned}F'(l,l+1) = &-F(l,l+1)\left[\frac{C'_{l+1}}{C_{l+1}}+\frac{C'_l}{C_l}+2P_d\right]+\frac{P_m}{2}\left[\frac{C_{l-1}}{C_l}F(l-1,l+1)+\frac{C_{l+2}}{C_{l+1}}F(l,l+2)-2F(l,l+1)\right]\\ &+\frac{P_p}{2}\left\{\frac{1}{C_l}+\frac{1}{C_{l+1}}-2F(l,l+1)+\frac{C_{l-1}}{C_l(1-C_l)}[1-C_lF(l,l+1)][1-C_lF(l,l-1)]F(l-1,l+1)\right.\\ &\left.+\frac{C_{l+2}}{C_{l+1}(1-C_{l+1})}[1-C_{l+1}F(l,l+1)][1-C_{l+1}F(l+1,l+2)]F(l,l+2)\right\}. \end{aligned}\tag{A7}$$

For any general distance $F(l,m)$, where $|l-m|>1$, we obtain

$$
\begin{aligned}
F'(l,m) = -F(l,m)\left[\frac{C_l'}{C_l} + \frac{C_m'}{C_m} + 2P_d\right] + \frac{P_m}{2}\left[\frac{C_{l-1}}{C_l}F(l-1,m) + \frac{C_{l+1}}{C_l}F(l+1,m)\right.\\
\left. + \frac{C_{m-1}}{C_m}F(l,m-1) + \frac{C_{m+1}}{C_m}F(l,m+1) - 4F(l,m)\right]\\
+\frac{P_p}{2}\left\{\frac{C_{l-1}}{C_l(1-C_l)}[1-C_lF(l,l-1)][1-C_lF(l,m)]F(m,l-1)\right.\\
+\frac{C_{l+1}}{C_l(1-C_l)}[1-C_lF(l,l+1)][1-C_lF(l,m)]F(m,l+1)\\
+\frac{C_{m+1}}{C_m(1-C_m)}[1-C_mF(l,m)][1-C_mF(m,m+1)]F(l,m+1)\\
\left.+\frac{C_{m-1}}{C_m(1-C_m)}[1-C_mF(l,m)][1-C_mF(m,m-1)]F(l,m-1)\right\}. \qquad \text{(A8)}
\end{aligned}
$$

4. Numerical solution

The solution of the systems of coupled nonlinear differential equations presented throughout the paper are generated numerically using a fourth-order Runge-Kutta method with constant time step h [25]. All numerical results presented in the manuscript are for $h = 1 \times 10^{-1}$. To test the accuracy of these numerical solutions we also generated results with $h = 1 \times 10^{-2}$ and demonstrated (results not shown) that they were visually indistinguishable from the results for $h = 1 \times 10^{-1}$.

[1] B. Berkowitz and H. Scher, Phys. Rev. E **57**, 5858 (1998).
[2] Y. Edery, H. Scher, and B. Berkowitz, Water Resour. Res. **46**, W07524 (2010).
[3] R. Law, D. J. Murrel, and U. Dieckmann, Ecology **84**, 252 (2003).
[4] D. J. Murrell, U. Dieckmann, and R. Law, J. Theor. Biol. **229**, 421 (2004).
[5] M. Raghib, N. A. Hill, and U. Dieckmann, J. Math. Biol. **62**, 605 (2011).
[6] C. Deroulers, M. Aubert, M. Badoual, and B. Grammaticos, Phys. Rev. E **79**, 031917 (2009).
[7] A. Fernando, K. A. Landman, and M. J. Simpson, Phys. Rev. E **81**, 011903 (2010).
[8] M. J. Simpson, K. A. Landman, and B. D. Hughes, Physica A **388**, 399 (2009).
[9] M. J. Simpson, K. A. Landman, and B. D. Hughes, Phys. Rev. E **79**, 031920 (2009).
[10] M. J. Simpson, K. A. Landman, and B. D. Hughes, Physica A **389**, 3779 (2010).
[11] M. J. Simpson, C. Towne, D. L. S. McElwain, and Z. Upton, Phys. Rev. E **82**, 041901 (2010).
[12] M. J. Simpson, R. E. Baker, and S. W. McCue, Phys. Rev. E **83**, 021901 (2011).
[13] K. Anguige and C. Schmeiser, J. Math. Biol. **58**, 395 (2009).
[14] R. E. Baker and M. J. Simpson, Phys. Rev. E **82**, 041905 (2010).
[15] T. M. Liggett, *Stochastic Interacting Systems: Contact, Voter and Exclusion Processes* (Springer, New York, 1999).
[16] T. Callaghan, E. Khain, L. M. Sander, and R. M. Ziff, J. Stat. Phys. **122**, 909 (2006).
[17] J. Mai, V. N. Kuzovkov, and W. J. von Niessen, Chem. Phys. **98**, 10017 (1993).
[18] J. Mai, V. N. Kuzovkov, and W. von Niessen, Physica A **203**, 298 (1994).
[19] N. N. Bugaenko, A. N. Gorban, and I. V. Karlin, Theor. Math. Phys. **88**, 977 (1991).
[20] A. Singer, J. Chem. Phys. **121**, 3657 (2004).
[21] P. K. Maini, D. L. S. McElwain, and D. Leavesley, Appl. Math. Lett. **17**, 575 (2004).
[22] P. K. Maini, D. L. S. McElwain, and D. I. Leavesley, Tissue Eng. **10**, 475 (2004).
[23] G. H. A. Cole and A. Moreton, Mol. Phys. **13**, 501 (1967).
[24] G. H. A Cole, Rep. Prog. Phys. **31**, 419 (1968).
[25] S. C. Chapra and R. P. Canale, *Numerical Methods for Engineers* (McGraw-Hill, Singapore, 1998).